GEOCHEMISTRY

Postmelting hydrogen enrichment in the oceanic lithosphere

Veronique Le Roux[1]*, Benjamin M. Urann[1,2], Daniele Brunelli[3,4], Enrico Bonatti[4,5], Anna Cipriani[3,5], Sylvie Demouchy[6], Brian D. Monteleone[1]

The large range of H_2O contents recorded in minerals from exhumed mantle rocks has been challenging to interpret, as it often records a combination of melting, metasomatism, and diffusional processes in spatially isolated samples. Here, we determine the temporal variations of H_2O contents in pyroxenes from a 24-Ma time series of abyssal peridotites exposed along the Vema fracture zone (Atlantic Ocean). The H_2O contents of pyroxenes correlate with both crustal ages and pyroxene chemistry and increase toward younger and more refractory peridotites. These variations are inconsistent with residual values after melting and opposite to trends often observed in mantle xenoliths. Postmelting hydrogen enrichment occurred by ionic diffusion during cryptic metasomatism of peridotite residues by low-degree, volatile-rich melts and was particularly effective in the most depleted peridotites. The presence of hydrous melts under ridges leads to widespread hydrogen incorporation in the oceanic lithosphere, likely lowering mantle viscosity compared to dry models.

INTRODUCTION

The incorporation of crystallographically bonded hydrogen (also referred to as H_2O or water) as atomic impurity in mantle minerals plays a key role in mantle dynamics (*1*–*4*). However, the mechanisms that control H_2O distribution in upper mantle rocks remain poorly understood. Most of the current constraints on H_2O distribution in exhumed mantle rocks come from xenoliths. These rocks typically sample a cold, variably oxidized, fluid-rich lithospheric mantle (*5*) and may not be representative of asthenospheric conditions. Previous studies have shown that pyroxenes hold most of the H_2O budget of nominally anhydrous peridotites, but significant variations are observed (*6*–*8*). For example, xenolithic orthopyroxene (opx) contain from <10 to 400 μg g^{-1} H_2O, while H_2O in xenolithic clinopyroxene (cpx) range from <10 to 900 μg g^{-1} H_2O (*6*, *7*). Deciphering the processes that control these variations remains a challenge because well-defined correlations between H_2O and major or trace elements are rarely found (*9*, *10*). In some xenoliths, H_2O in pyroxene correlates with major elements (e.g., Al), as experimentally predicted (*11*), but abundances are often too high to represent a partial melting residue, complicating the reconstruction of mantle H_2O budgets (*6*).

Abyssal peridotites are mantle residues left after mid-ocean ridge basalt extraction from the asthenospheric mantle (*12*), now emplaced in the lithosphere and uplifted tectonically to the seafloor. Their constituent minerals (olivine, opx, and cpx) have only been analyzed for H_2O and other volatiles in a limited number of studies (*13*–*16*), likely because their significant alteration represents a technical challenge. Earlier studies on abyssal peridotites have reported variations in the H_2O contents of pyroxenes, interpreted to reflect residual H_2O contents of the oceanic upper mantle (*15*) and/or H_2O addition after partial melting (*14*, *15*). It was also argued that the H_2O content of pyroxene minerals from the Southwest Indian Ridge and Hess Deep, East Pacific Rise, may have been modified after initial melt extraction (*13*, *17*). Although these studies provide information on H_2O variability in abyssal peridotites, most of the samples are spatially isolated and sometimes lack a broader tectonic context. Therefore, this study focuses on a time series of genetically related abyssal peridotites to untangle the processes that control H_2O distribution over time and determine how they compare to xenoliths.

In particular, we use secondary ion mass spectrometry (SIMS) to measure the in situ volatile contents (in particular H_2O and F) of opx and cpx in abyssal peridotites from the Vema fracture zone (11°N; Equatorial Atlantic). The Vema lithospheric section (VLS) exposes a >300-km-long, ~1-km-thick segment of lithospheric mantle overlain by oceanic crust made of gabbros, dykes, and basalts (*18*). The peridotite samples used in this study were collected every 10 to 20 km along the VLS and span crustal ages from 1.5 to 24 million years (Ma) (*18*, *19*). Crustal ages were estimated from geomagnetic time scales (*20*) and U-Pb ages in crustal gabbros (*21*). The time at which peridotite was emplaced into the lithosphere is estimated using the crustal age and the spreading rate, considering the delay of emplacement between basalts and its parent peridotite (*18*, *19*). The degree of melting in peridotites along the VLS increases toward younger crustal ages, from 8 to 14% on average (*18*, *19*, *22*). Lower degrees of melting recorded in the older peridotites (>15 Ma) may reflect undercooling of the peridotite mantle due to the presence of pyroxenite in the source (*23*). Crustal thickness increased over time from 4.8 ± 0.2 km to 5.4 ± 0.2 km (*18*, *19*), concomitant with a decrease in full spreading rates from ~35 to 27 mm $year^{-1}$ (*18*). The peridotite time series used in this study have porphyroclastic, protogranular, and/or occasionally mylonitic textures and were all equilibrated in the spinel stability field. Amphibole is sometimes present in peridotites along the VLS (*24*), but none of the samples investigated here contain amphibole. The samples are typically 70 to 80% altered, with variably large (2-mm- to >1-cm-diameter) relic pyroxene, and small (<500-μm-diameter) relic cores of olivine in some of the samples (*19*, *22*). This study combines volatile measurements with selected trace and major element analyses in pyroxenes to elucidate the processes that control H_2O variations in peridotite

[1]Department of Geology and Geophysics, Woods Hole Oceanographic Institution, Woods Hole, MA 02543, USA. [2]MIT-WHOI Joint Program, Marine Geology and Geophysics, Woods Hole Oceanographic Institution, Woods Hole, MA 02543, USA. [3]Dipartimento di Scienze Chimiche e Geologiche, Università di Modena e Reggio Emilia, Modena, Italy. [4]Istituto di Scienze Marine, CNR, Bologna, Italy. [5]Lamont Doherty Earth Observatory, Columbia University, New York, NY 10027, USA. [6]Géosciences Montpellier, Université Montpellier & CNRS, Montpellier, France.
*Corresponding author. Email: vleroux@whoi.edu

from ridge settings. Last, we discuss the implications of hydrogen incorporation in residual abyssal peridotites for the viscosity of the oceanic lithosphere.

RESULTS

Volatile distribution in VLS pyroxenes

SIMS analyses were performed in 31 VLS cpx and 31 VLS opx (including 28 samples with both opx and cpx data), resulting in a total of 235 analyses after filtering for data quality (see the Supplementary Materials for details). Average H_2O and fluorine contents in opx vary from 81 to 362 μg g^{-1} and 0.15 to 21 μg g^{-1}, respectively, while average H_2O and fluorine contents in cpx vary from 189 to 724 μg g^{-1} and 0.25 to 51 μg g^{-1}, respectively (table S1). No systematic hydrogen loss or gain from cores to rims is observed as a function of crustal ages, but cpx H_2O abundances are slightly more scattered from the 1:1 line compared to the opx (Fig. 1). Fluorine core-to-rim concentrations show tight correlations in both opx and cpx, with limited deviation from the 1:1 line.

The distribution of H_2O between cpx and opx ($D_{H_2O}^{cpx/opx}$) has been reported in a large number of studies on natural peridotites (*7*, *13*) and experimental samples (*25*). Data from this study are reported in Fig. 2 along with data from the literature. H_2O partitions preferentially into cpx over opx. Natural samples (mantle xenoliths and oceanic peridotites) show more H_2O enrichment in cpx over opx ($D_{H_2O}^{cpx/opx}$ = 2.6 ± 0.9) compared to experimental samples ($D_{H_2O}^{cpx/opx}$ = 1.3 ± 0.3) (*13*). The VLS pyroxene data also exhibit this difference to experimental data, with a $D_{H_2O}^{cpx/opx}$ of 2.3 ± 0.3 (1SD, N = 28) consistent with $D_{H_2O}^{cpx/opx}$ of 2.4 ± 0.3 previously reported for oceanic peridotites only (*13*). A preliminary Fourier transform infrared spectroscopy (FTIR) study of VLS pyroxenes from 10 to 19 Ma (*14*) yielded an average $D_{H_2O}^{cpx/opx}$ of 3.1 ± 0.6, higher than most natural peridotites. Data for fluorine partitioning are significantly scarcer for both natural and experimental samples. In the VLS pyroxenes, we find an average $D_F^{cpx/opx}$ of 2.2 ± 1, similar to what has been found in a limited set of natural and experimental samples ($D_F^{cpx/opx}$ of 2.4 ± 1.3) (*26*). No systematic variation in $D_{H_2O}^{cpx/opx}$ and $D_F^{cpx/opx}$ is observed with crustal ages.

Volatile variations with crustal ages and degree of depletion

Crustal ages and H_2O contents of opx and cpx are negatively correlated (Fig. 3). The H_2O contents of cpx and opx increase toward younger crustal ages and are about two times higher in the <10-Ma interval compared to the 20- to 24-Ma interval. A previous VLS FTIR study (*14*) reported weak to no correlation (R^2 = 0.06 to 0.23), possibly due to limited sample availability. On the other hand, fluorine shows two distinct trends. Opposite to H_2O, fluorine

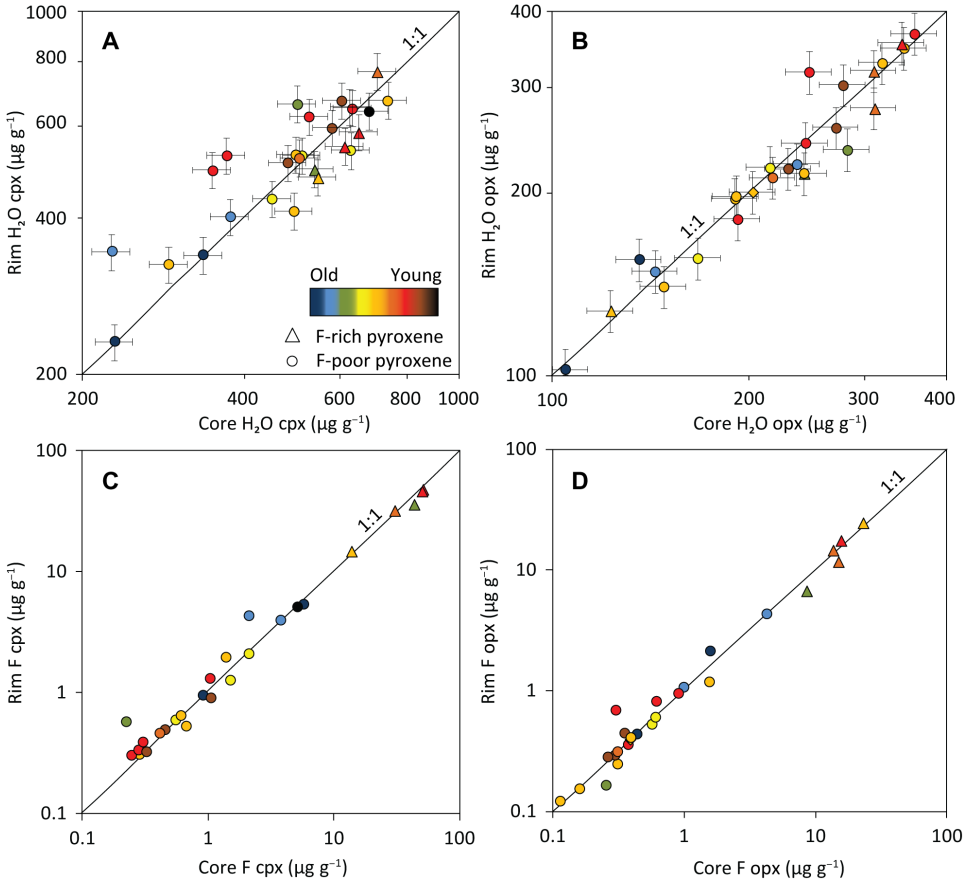

Fig. 1. Core-to-rim variations of H_2O and F (μg g^{-1}) in pyroxenes. H_2O in (**A**) cpx rims versus cores (R^2 = 0.66) and (**B**) opx rims versus cores (R^2 = 0.88), and F in (**C**) cpx rims versus cores (R^2 = 0.99) and (**D**) opx rims versus cores (R^2 = 0.97). Color code refers to associated crustal ages. Each point represents one analysis. Error bars are typical propagated 2 SE of individual analyses (internal error and propagated error from calibration curve; see the Supplementary Materials) and smaller than symbols when not apparent. F-rich cpx (>10 μg g^{-1}) and F-rich opx (>4 μg g^{-1}) appear as triangles.

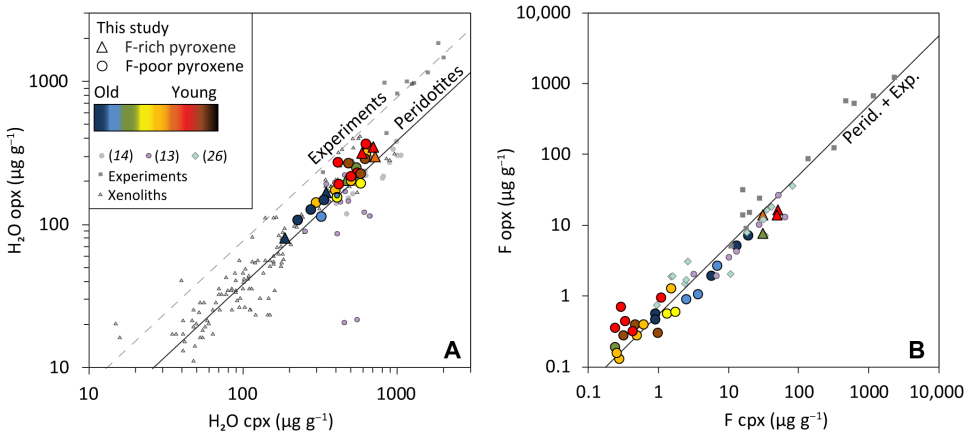

Fig. 2. Covariations of H_2O and F (μg g^{-1}) in pyroxenes. (**A**) H_2O in opx versus cpx from this study ($R^2 = 0.80$) compared to experimental studies (*11*, *25*, *39*), xenoliths (*7*), and other oceanic peridotites (*13*, *14*). (**B**) F in opx versus cpx from this study ($R^2 = 0.95$) compared to experimental studies (*11*, *69*) and peridotitic pyroxenes from various tectonic environments (*26*). Error bars are omitted for clarity. Color code refers to associated crustal ages. Each point represents the average of all grains in one sample. F-rich cpx (>10 μg g^{-1}) and F-rich opx (>4 μg g^{-1}) appear as triangles.

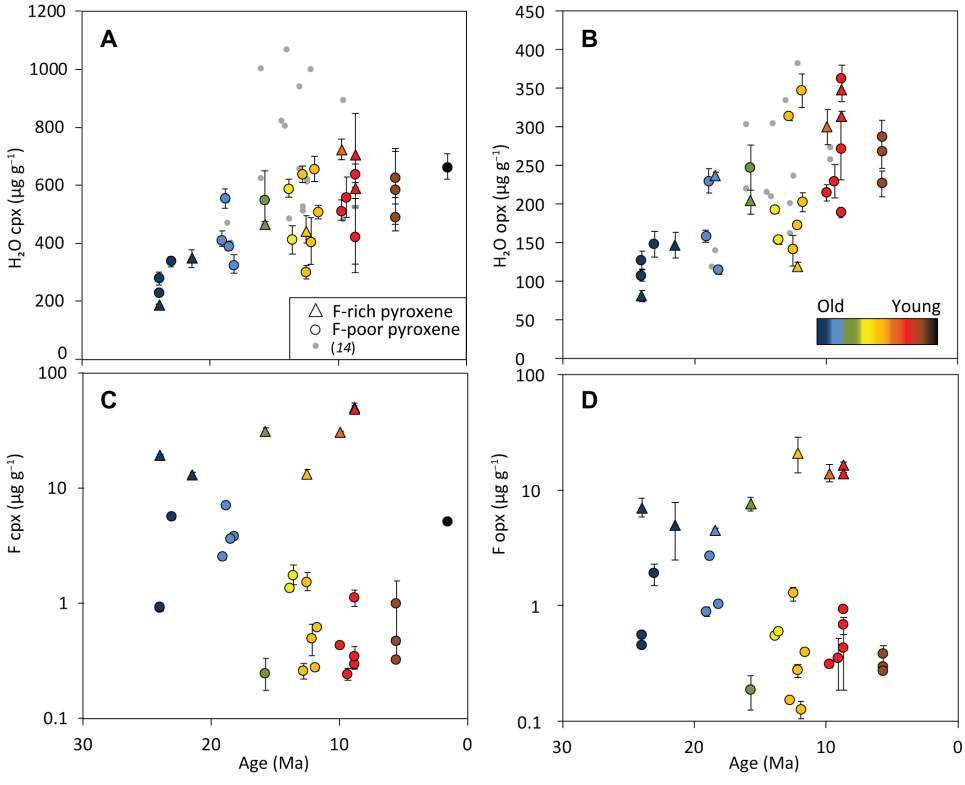

Fig. 3. H_2O and F (μg g^{-1}) in pyroxenes over 23-Ma time series. (**A**) H_2O in cpx and (**B**) in opx versus crustal ages ($R^2 = 0.52$ and 0.43, respectively). Note that the *x* axis is reversed to reflect older rocks in the West compared to the East. Error bars are omitted for clarity for a previous FTIR study (*14*). (**C**) F in cpx and (**D**) in opx versus crustal ages. F-rich cpx (>10 μg g^{-1}) and F-rich opx (>4 μg g^{-1}) appear as triangles. In (C), R^2 values for F-poor and F-rich samples are 0.1 and 0.51, respectively. In (D), R^2 values for F-poor and F-rich samples are 0.2 and 0.61, respectively. Error bars for volatiles are 2 SE of sample averages and smaller than symbols when not apparent; each point represents the average of all grains in one sample. Color code refers to associated crustal ages.

concentrations in both pyroxenes generally decrease toward younger crustal ages, except in the few fluorine-rich samples (triangle symbols) where F concentrations are high (>10 μg g^{-1} for cpx and >4 μg g^{-1} for opx) and follow a reverse trend. High abundances of F do not reflect analytical artifacts or the presence of mineral inclusions, as high F concentrations are found throughout each grain in both opx and cpx from the same samples.

Broad correlations are also found between the degree of melting recorded by the peridotites and pyroxene volatile contents (Fig. 4). The degree of melting in VLS peridotites increases toward younger

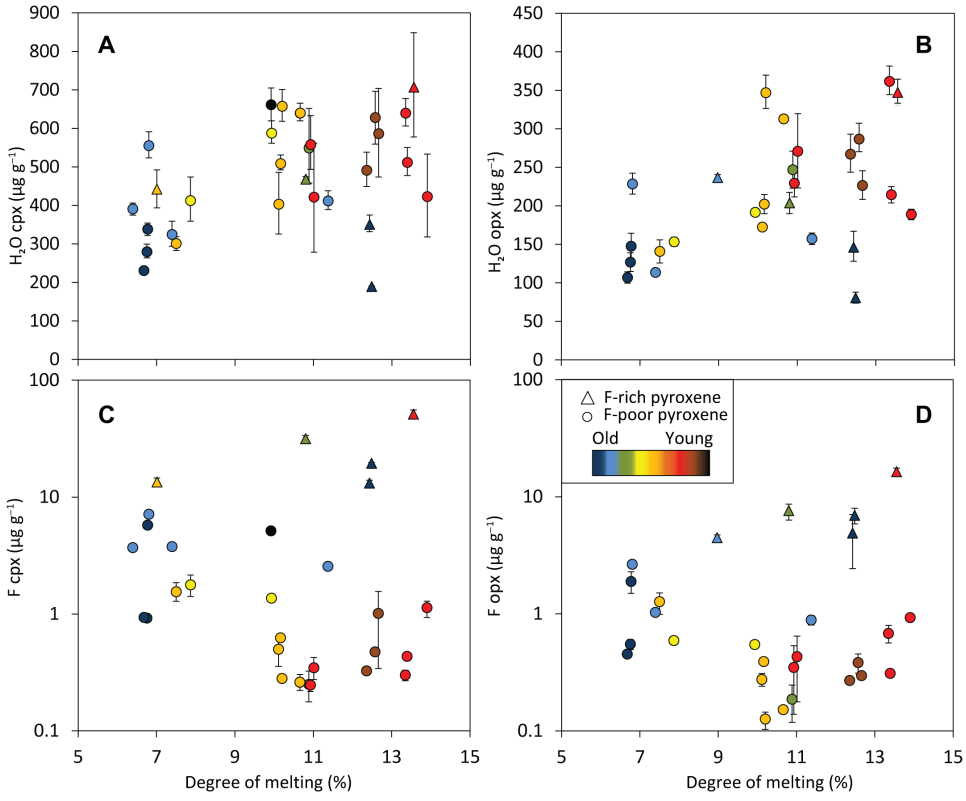

Fig. 4. H_2O and F (µg g^{-1}) in pyroxenes versus degree of melting of peridotites. (**A**) H_2O in cpx and (**B**) in opx versus melting degree. R^2 values are 0.19 and 0.21, respectively. (**C**) F in cpx and (**D**) in opx versus melting degree. In (C), R^2 values for F-poor and F-rich samples are 0.32 and 0.27, respectively. In (D), R^2 values for F-poor and F-rich samples are 0.26 and 0.42, respectively. Error bars for volatiles are 2 SE of sample averages and smaller than symbols when not apparent; each point represents the average of all grains in one sample. Color code refers to associated crustal ages. F-rich cpx (>10 µg g^{-1}) and F-rich opx (>4 µg g^{-1}) appear as triangles.

crustal ages, as shown by previous studies (*18*, *19*, *22*). For consistency between previous studies, the degree of melting was recalculated using spinel compositions only (*27*). The degree of melting in the source correlates broadly with the H_2O contents of opx and cpx, whereby the more depleted pyroxenes contain the highest H_2O contents. On the other hand, fluorine decreases with increasing degrees of melting in fluorine-poor pyroxenes, while data are too limited in fluorine-rich pyroxenes to assess the effect of melting.

Volatile variations with pyroxene chemistry

As observed in a previous study of abyssal peridotites (*13*), H_2O in pyroxene does not correlate with tetrahedrally or octahedrally coordinated Al^{3+} (fig. S1). This behavior is opposite to experimental predictions after partial melting (*11*) and to elemental trends observed in some xenoliths (*28*). Further, H_2O negatively correlates with Ti and Na in both pyroxenes (Fig. 5). Opposite to that trend, fluorine positively correlates with Ti and Na in both cpx and opx in fluorine-poor samples (fig. S2). The few fluorine-rich samples, however, show negative correlations between F, Ti, and Na.

In addition to major elements, H_2O and fluorine covary with other incompatible trace elements (Figs. 5 and 6). In particular, H_2O negatively correlates with rare earth elements (REE) Sm, Gd, and Yb and, despite a partitioning behavior close to Ce (*29*), shows the strongest negative correlation with mid-REE Gd. H_2O concentrations in cpx increase with decreasing Gd/Yb normalized to chondrite (*30*) in cpx. Similarly, in fluorine-rich samples, fluorine displays negative correlations with REE and positive correlations with H_2O (Fig. 6). In contrast, fluorine abundances in fluorine-poor samples display broad positive correlations with REE and a broad negative correlation with H_2O.

DISCUSSION

Tracers of partial melting and their relationship to H_2O and fluorine

Incompatible trace elements, such as normalized (*30*) Sm/Yb and Yb in VLS cpx, follow residual trends after partial melting. Figure 6 illustrates that REE variability in VLS cpx can be explained by fractional melting of a depleted MORB (mid-ocean ridge basalt) mantle (DMM) in the garnet stability field, followed by fractional melting of DMM in the spinel stability field. Melting parameters (*11*, *25*, *26*, *31*–*34*) are reported in table S2 and follow the method described in previous studies (*22*, *35*). A mantle source that contains ~10 µg g^{-1} F (*26*) and melted less than 20% would yield residual fluorine and REE abundances within the range observed in this study.

On the other hand, H_2O displays negative correlations with major and trace elements predicted to behave similarly to H_2O during partial melting. The H_2O variations in VLS pyroxenes cannot be explained solely by partial melting, whether the source is typical DMM (~100 to 200 µg g^{-1} H_2O) (*32*) or more H_2O-rich. Similarly, some pyroxenes contain too much fluorine to represent residues after partial melting. Stochastic F enrichments are unlikely to have been produced during

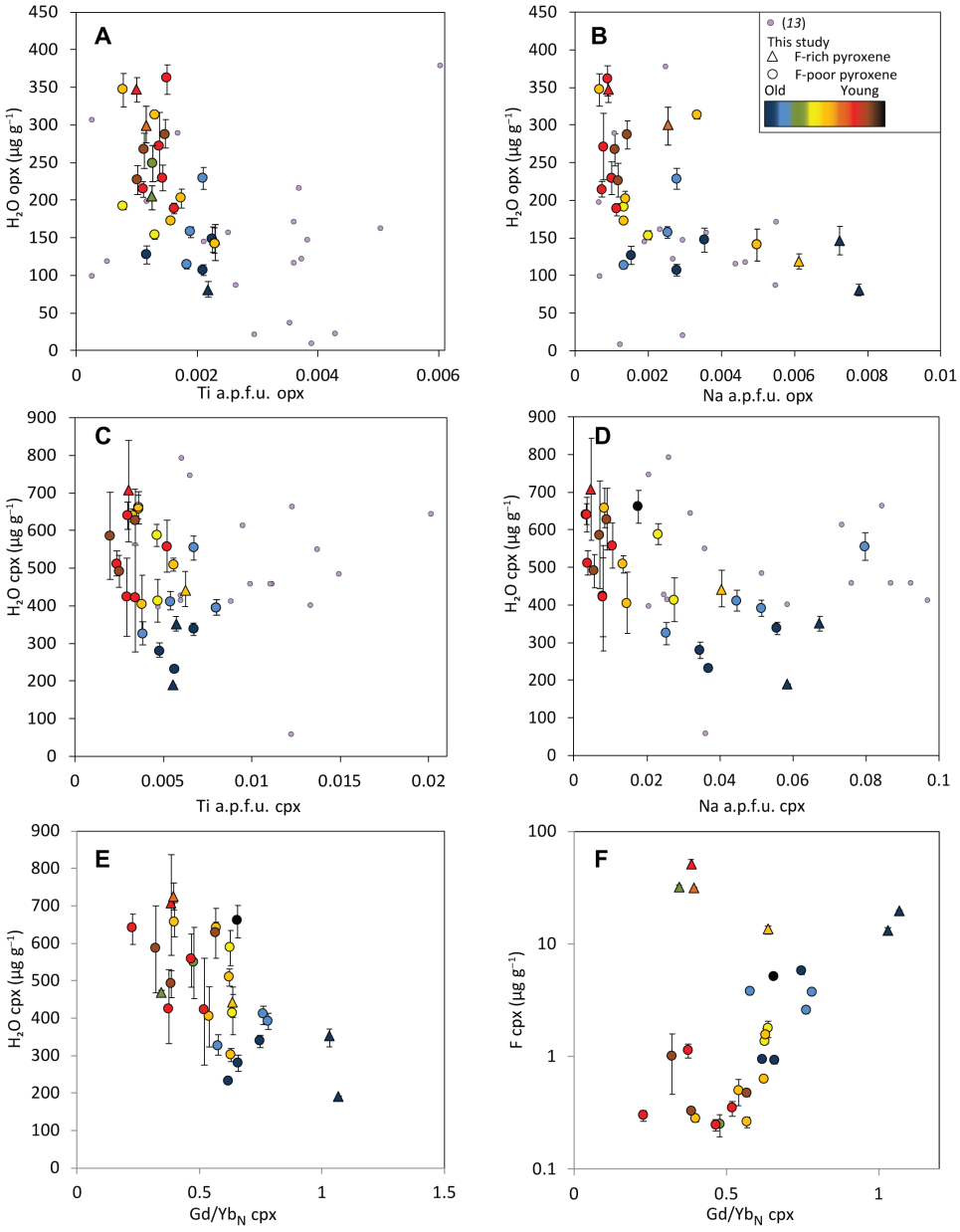

Fig. 5. H_2O and F (μg g^{-1}) versus minor and trace elements in pyroxenes. H_2O versus (**A**) Ti in atoms per formula unit (a.p.f.u.) ($R^2 = 0.36$) and (**B**) Na a.p.f.u. in opx ($R^2 = 0.39$), (**C**) H_2O versus Ti a.p.f.u. ($R^2 = 0.25$), and (**D**) Na a.p.f.u. in cpx ($R^2 = 0.52$). (**E**) H_2O versus Gd/Yb_N (*30*) in cpx ($R^2 = 0.37$) and (**F**) F versus Gd/Yb_N in cpx (R^2 values for F-poor and F-rich samples are 0.50 and 0.62, respectively). Error bars for volatiles are 2 SE of sample averages and smaller than symbols when not apparent; each point represents the average of all grains in one sample. Color code refers to associated crustal ages. F-rich cpx (>10 μg g^{-1}) and F-rich opx (>4 μg g^{-1}) appear as triangles.

modal metasomatism because elements that are typically enriched during melt metasomatism (e.g., REE, Na, and Ti) negatively correlate with fluorine. Instead, the positive correlation between fluorine and hydrogen in F-rich samples (Fig. 6) could indicate that F-H incorporation occurred as a complex defect similar to mechanism observed in olivine (*36*) and that F enrichment resulted from localized cryptic metasomatism by a F-rich fluid. This fluid could have originated in a subridge magma chamber and sporadically percolated overlying peridotites during their emplacement at shallow levels. Although the reason for high fluorine abundances in selected pyroxenes remains to be fully understood, these observations cast doubt on the ability to use fluorine as a direct tracer of H_2O in peridotite minerals (*13*).

Effects of serpentinization and subsolidus re-equilibration on pyroxene H_2O contents

H_2O variations are about two times higher in depleted pyroxenes compared to fertile ones, yet petrographic observations do not indicate significant differences in H_2O contents linked to degree of alteration or changes in microstructure such as grain size. FTIR spectra obtained on a subset of serpentinite-free grains (*14*) are broadly consistent with SIMS results, and negative correlations between

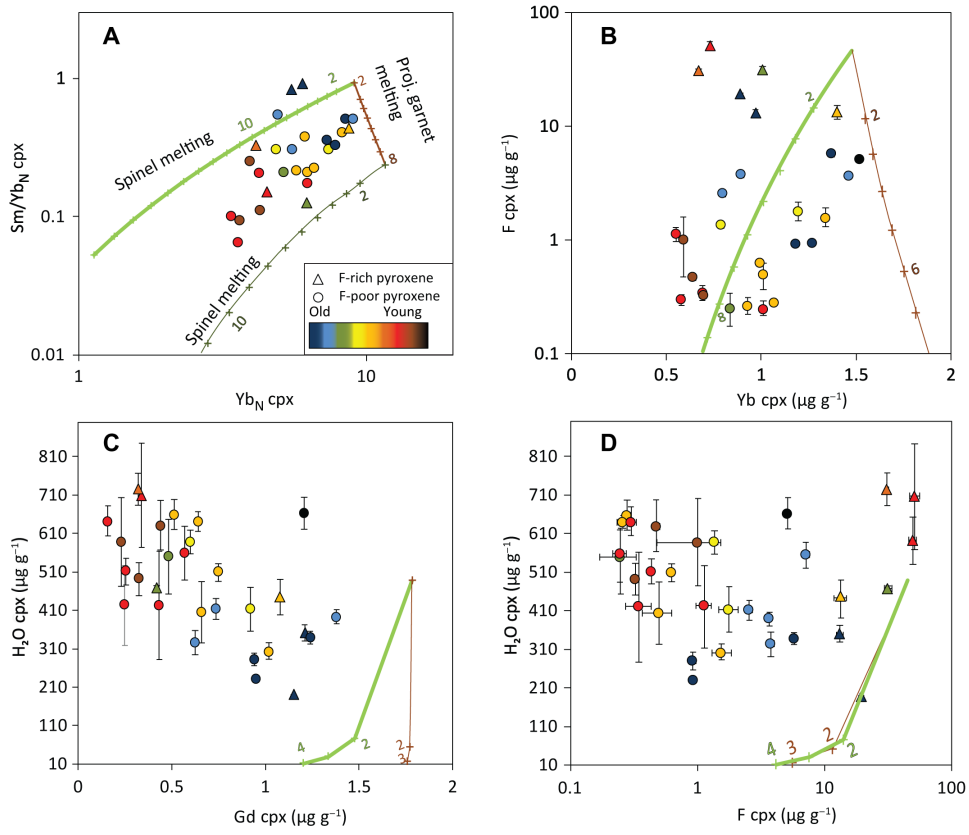

Fig. 6. Volatile and trace element variations compared to fractional melting model of DMM (*31*). (**A**) Sm/Yb$_N$ in cpx versus Yb$_N$ in cpx (*30*) compared to spinel-field melting (thick light green) and projected garnet-field melting (*22*) (brown trend) followed by spinel-field melting (dark green). Small colored numbers next to cross symbols indicate the degree of melting. The source is assumed to have 16 μg g^{-1} F and 142 μg g^{-1} H$_2$O (*32*). (**B**) F in cpx (μg g^{-1}) versus Yb in cpx (μg g^{-1}), compared to the melting models. R^2 values for F-poor and F-rich samples are 0.16 and 0.50, respectively. (**C**) H$_2$O versus Gd (μg g^{-1}) in cpx (R^2 = 0.34) compared to the melting models. Mid-REEs display the best inverse correlations with H$_2$O. (**D**) H$_2$O versus F (μg g^{-1}) in cpx compared to the melting models. R^2 values for F-poor and F-rich samples are 0.02 and 0.51, respectively. Error bars for volatiles are 2 SE of sample averages and smaller than symbols when not apparent; each point represents the average of all grains in one sample. Color code refers to associated crustal ages. F-rich cpx (>10 μg g^{-1}) and F-rich opx (>4 μg g^{-1}) appear as triangles.

H$_2$O and other incompatible elements are not expected during serpentinization. In addition, no large core to rim variations are observed, inconsistent with transient serpentinization. Last, hydrogen diffusivities at serpentinization temperatures may be too low to affect primary H$_2$O abundances in pyroxenes, although this is still debated (*37*).

Previous studies have reviewed the effects of depth and pressure on H partition coefficients between olivine and opx for peridotites equilibrated in the spinel and garnet stability field. Natural pyroxenes and bulk peridotites from global datasets display order of magnitude variations in H$_2$O contents at similar pressures of equilibration in the spinel stability field (*7*), casting doubt that pressure is the main controller of hydrogen distribution in the oceanic lithospheric mantle. In addition, a broad increase in $D_{H_2O}^{ol/opx}$ can be observed in cratonic peridotites equilibrated at depths of >150 km, but no systematic variations are observed in the spinel stability field (*7*). Thus, the potential effects of pressure of melting and/or equilibration are likely overprinted by other processes in the shallow oceanic lithospheric mantle. Further, hydrogen redistribution during cooling has been inferred to explain the discrepancy (*38*) in $D_{H_2O}^{cpx/opx}$ between natural samples (average of 2.4; samples typically equilibrated at <1000°C) (*13*) and experiments (average of 1.3; samples typically equilibrated at >1200°C) (*25*, *38*, *39*). Temperatures of equilibration of VLS peridotites were calculated using major element composition of opx and cpx (*40*, *41*) for an average pressure of 1.5 GPa, i.e., in the spinel stability field (*23*). Neither H$_2$O concentrations nor $D_{H_2O}^{cpx/opx}$ display correlations with temperatures of re-equilibration at subsolidus conditions (fig. S3). This observation comes with the caveat that H could have further diffused after closure of the major element systems. However, if H enrichments in VLS pyroxenes were primarily controlled by variable extents of subsolidus cooling, core-to-rim profiles may show disequilibrium distribution, and $D_{H_2O}^{cpx/opx}$ should vary systematically with crustal ages, with samples re-equilibrated at higher temperatures displaying a lower $D_{H_2O}^{cpx/opx}$. This is not observed in the VLS samples. Therefore, although subsolidus redistribution of hydrogen likely occurred before exhumation on the seafloor (because $D_{H_2O}^{cpx/opx}$ = 2.3), it cannot be the main mechanism behind the 24-Ma H$_2$O enrichment trend and had to be preceded by H enrichment in the bulk system. Subsolidus redistribution cannot provide enough H$_2$O to double concentrations over time in both pyroxenes, as this would not satisfy mass balance requirements. Therefore, an external reservoir of hydrogen (e.g., melt/fluid) is needed.

Hydrogen enrichment during melt metasomatism

Limited metasomatism has been reported in VLS peridotites, where 0.1 to 1% of residual melt could be trapped (*22*). Modal metasomatism leads to precipitation of new minerals from a migrating melt and produces concomitant enrichments of incompatible elements in newly crystallized pyroxenes (*42*). In that scenario, H_2O should positively correlate with REEs (e.g., La and Ce), Al, Na, and Ti, but the opposite is observed in the VLS pyroxenes. Therefore, hydrogen variations in the VLS time series do not primarily reflect modal metasomatism.

However, hydrogen alone could have diffused from these small melt fractions trapped at grain boundaries. Hydrogen diffuses at a faster rate than any other trace, minor, and major elements (*6*, *7*). Diffusivities of hydrogen in pyroxene (*43*–*45*) at temperatures of 1000 to 1200°C are in the range of ~10^{-12} to 10^{-10} m^2 s^{-1}. These diffusivities yield a minimal characteristic distance of <10 m/Ma compared to <0.6 mm/Ma for REE (*46*), assuming a diffusion coefficient of 10^{-21} m^2 s^{-1}. Considering that the peridotites were continuously percolated by basalts, while they ascended under the ridge from ~70- to 100-km depth (*23*) at a minimum rate of 1 m $year^{-1}$ for 70 to 100 ka, hydrogen could have diffused at least ~1 m in all peridotite samples, well above the observed grain size in these rocks. Therefore, while the trace and major element abundances of VLS pyroxenes primarily reflect partial melting (*22*), hydrogen concentrations record a superimposed gain of hydrogen that occurred by ionic diffusion during cryptic metasomatism.

Hydrogen can be incorporated in pyroxene both by coupled substitution mechanisms and by occupying metal vacancies, meaning that partition coefficients between pyroxene and melt are, in part, dictated by crystal chemistry and point defect populations (*25*, *34*, *44*, *47*–*49*). Point defect theory predicts that hydrogen incorporation is favored by increasing concentration of intrinsic as well as extrinsic (minor and trace elements) point defects (*9*, *50*, *51*). Vacancies are the most common type of point defects that can be hydrogenated, and their concentrations typically increase with increasing temperature, oxygen fugacity (fO_2), and concentrations of trace elements (*52*), particularly trivalent impurities. Pyroxenes that contain high H_2O abundances can record more reducing conditions than H_2O-poor pyroxenes (*53*, *54*). This has been linked to the incorporation of hydrogen via the proton-polaron exchange reaction (*55*) or variations of that reaction (*56*), resulting in reduction of Fe^{3+} to Fe^{2+}. Seafloor abyssal peridotites record some of the lowest mantle fO_2 observed for spinel peridotites (*57*), which could favor the large uptake of hydrogen observed in the VLS time series. Although accurate fO_2 calculations would require olivine and corrected Fe^{3+} spinel data (*58*), these reactions are favored under reducing conditions and the presence of lattice vacancies related to Fe^{3+}. As the mantle composition at the VLS changed from a (potentially oxidized) pyroxenite-bearing source to a (potentially more reduced) peridotite (*23*), it is possible that the source composition influenced hydrogen uptake. It could also be speculated that the loss of incompatible trace elements during melting could create transient vacancies and opportunities for elemental substitutions with H, favored by a short time lapse between melting and subsequent metasomatism under ridges. This increase in vacancy concentrations could favor additional H incorporation (*59*). Associated substitutions may include replacement of Na^+ (lost during melting) by similarly charged H^+, as suggested for olivine (*60*) and supported by negative correlations between Na and H_2O in the VLS pyroxenes (Fig. 5).

To our knowledge, the reverse correlations between H_2O abundances in pyroxenes and the degree of depletion in the residual mantle at the VLS have not been observed in mantle xenoliths. Depending on the mechanism of hydrogen incorporation, xenoliths can show positive (*56*) or negative (*54*) correlations between H_2O and fO_2 so that oxidizing conditions under which xenoliths evolve are not a prediction for their water contents. Although mantle xenoliths are prone to melt-rock reactions (*5*), some retain broad positive correlations between H_2O and other incompatible elements (*28*, *61*), opposite to the VLS time series. It is possible that, in xenoliths, a loss of Na^+ during melting would not necessarily be followed by H^+ addition from a percolating melt, as samples may re-equilibrate in the lithospheric mantle for millions of years before metasomatism and/or eruption occurs.

Hydrous melts under ridges

Only a fluid or melt occurring on a large scale could create the trends seen in the 24-Ma time series. Therefore, volatile-rich melts must occur under ridges, at least in the vicinity of fracture zones and potentially elsewhere. The H_2O contents of equilibrium melts are calculated using experimentally determined pyroxene-melt partition coefficients [$D_{H_2O}^{cpx/melt}$ of 0.016; (*11*, *25*)] and cpx H_2O abundances. Lacking olivine measurements, we apply a first-order correction factor of 1.4 to the measured H_2O abundances in cpx, which corresponds to the average correction factor reported for samples equilibrated at ~900° to 1100°C (*38*, *41*) and similar to equilibrium temperatures reported here (table S1). For example, a cpx that contains 545 μg g^{-1} H_2O after subsolidus re-equilibration would be assumed to contain only 389 μg g^{-1} H_2O at mantle conditions. The equilibrium hydrous melt contains ~1.6 weight % (wt %) H_2O in the older portion of the VLS (>15 Ma) and ~2.4 wt % H_2O in the younger portion of the VLS (<15 Ma). This is significantly higher than the average MORB H_2O contents [0.2 wt % (*62*); MgO > 8 wt % only] and H_2O averages of VLS basalts (<0.3 wt % H_2O) (*62*). Although hydrous melts may be diluted by more abundant dry melts under ridges, hydrous melts (>1 wt % H_2O) have been observed in the vicinity of fracture zones (*63*). Numerical simulations also predict that low-degree, volatile-rich melts could be trapped in the lithospheric mantle under ridges (*64*). Hydrogen enrichment observed in large swaths of VLS peridotites support this hypothesis. In addition, crystallization of small melt fractions has been observed in most abyssal peridotites (*35*, *65*), and 0.1 to 1% of trapped melt may be present in the VLS peridotite residue (*22*). These melts, potentially trapped at grain boundaries (*66*), are ideal candidates to carry H and other incompatible elements, but only H may have enough time to re-equilibrate in the system. This is consistent with the observation that most abyssal peridotites are enriched in light REE (LREE) compared to their corresponding cpx (*67*), which can be explained by a late incompatible element enrichment at grain boundaries.

Water budget of abyssal peridotites and lithosphere viscosity

On the basis of our results, the bulk H_2O budget of VLS abyssal peridotites (unaltered primary assemblage) should be largely controlled by pyroxenes (>75%). Using a range of well-established partition coefficients between opx, cpx, and olivine (ol) at subsolidus and mantle conditions ($D_{H_2O}^{ol/opx}$ = 0.04 to 0.11; $D_{H_2O}^{ol/cpx}$ = 0.02 to 0.07) (*11*, *13*, *25*, *39*), a representative range of olivine and bulk abundances can be calculated. Modal compositions of typical abyssal peridotite (*27*)

(ol, 73%; opx, 22%; cpx, 4%; spinel, 1%) and depleted MORB mantle (*31*) (ol, 57%; opx, 28%; cpx, 13%; spinel, 2%) are combined with cpx and opx H_2O contents of 545 to 371 and 240 to 163 μg g^{-1} H_2O, respectively. This range corresponds to average H_2O values in pyroxenes for <15-Ma and >15-Ma VLS peridotites. Bulk (unaltered) primary assemblages of residual peridotites at the VLS should therefore contain 55 to 160 μg g^{-1} H_2O (table S3). In theory, residual oceanic peridotites should be dehydrated after melting (*4*). However, this first-order estimate indicates that the water contents of abyssal peridotites are systematically higher than predicted for a residual lithosphere, and high H_2O abundances do not just reflect local anomalies. In addition, olivine is the primary phase that controls the rheological properties of the mantle lithosphere. Residual olivine water contents equilibrated with H_2O-rich pyroxenes would range from 8 to 50 μg g^{-1}, assuming the full range of cpx H_2O reported for VLS peridotites. The presence of low-degree, volatile-rich melts in ridge settings should therefore affect the rheological properties of the residual oceanic lithosphere. These hydrous melts may rarely erupt but instead metasomatize the residual lithosphere under oceanic ridges (*64*) and reduce mantle rock viscosity compared to models of dry lithosphere (*4*). These observations point to a critical need to understand H_2O distribution in the oceanic lithospheric mantle from the perspective of abyssal peridotites, in particular in large swaths of genetically related samples.

MATERIALS AND METHODS

Secondary ion mass spectrometry

SIMS analyses were conducted at the Northeast National Ion Microprobe facility at the Woods Hole Oceanographic Institution on a Cameca IMS 1280. Opx and cpx separates, ranging from 3 mm to <500 μm, were mounted in crystal bound and polished down to 1-μm grit using a diamond solution. After extraction from the crystal bound, the polished separates were thoroughly cleaned with acetone and re-mounted in indium. The indium mounts were re-polished with 1-μm diamond solution. Indium mounts were cleaned with ethanol and deionized water to remove surface contamination, and then the mounts were placed in a vacuum oven to dry. Samples were gold-coated to ~160-nm thickness and placed into a vacuum chamber for storage until analysis. Samples were loaded into the instrument sample chamber at least 12 hours before analysis to allow adequate pump down time and achieve chamber pressures of no more than $\sim 5 \times 10^{-9}$ torr. At least three spots per grain were analyzed, typically combined with core-to-rim profiles on most grains when possible. Spot locations were chosen to avoid any visible crack, inclusion, or anomalous surface appearance. A primary $^{133}Cs^+$ beam of 5.0 to 7.5 nA was sputtered through the sample surface with a 30 μm by 30 μm raster and a 400-μm field aperture, allowing only transmission of ions from the innermost 5 μm by 5 μm of the beam crater. Secondary magnet mass calibration was done before each measurement with mass resolving power of >6000 ($m/\Delta m$ at 10% peak height). We measured $^{12}C/^{30}Si$, $^{16}O^1H/^{30}Si$, $^{19}F/^{30}Si$, ($\pm^{31}P/^{30}Si$), $^{32}S/^{30}Si$, and $^{35}Cl/^{30}Si$ ratios in glass reference materials D51-3, D52-5, ALV519-4-1, 46D, 1649-3, 1654-3 6001, and AII107-D20 to produce a calibration slope for each 1-week analytical session (example calibration curves in fig. S4). Calibration slopes (m) were obtained by plotting measured isotope ratios (x) against known reference material concentrations (y) of the form $y = mx$ for each element of interest. Sample unknowns were then calculated by multiplying measured ratios by m. Calibration slope uncertainties were assessed using a bootstrapping technique (5000 iterations) to derive 95% confidence intervals, with the intercept set to zero. The bootstrapping code performs a nonlinear maximum likelihood inversion of a straight line to x and y data, where x and y are considered random variables with known errors. SD for glasses is based on multiple sessions over the years and is conservatively estimated to be $2\sigma = 10\%$; SDs for individual pyroxene reference materials were reported in a previous study (*68*). Points that constitute the calibration curve are randomly sampled 5000 times to generate confidence limits of parameter estimates. The glass calibration slope was used to reduce data for C, P, S, and Cl. Analytical uncertainties over five counting cycles were combined with calibration slope uncertainties to yield typical total uncertainty (2 SE, 95% confidence intervals) of <12, <12, <8, and <9% for C, P, S, and Cl, respectively. For reference, total uncertainties for OH and F in glass reference materials are <4 and <3%, respectively. Because volatile measurements on the SIMS are often affected by matrix effects, we also measured the same volatile elements on opx-cpx reference materials requested from the Department of Minerals Sciences, Smithsonian Museum (USA) and calibrated using mount NMNH 118331. Opx reference materials that were used for the calibration curve included NMNH 116610-29, 117322-245, 116610-5, and 109426-1. Cpx reference materials that were used for the calibration curve included NMNH 117213-5, 11610-18, 116610-15, 118317-1 (KH03-27), and 118318 (SC-J1). These reference materials have been calibrated for SIMS in a previous study using reference materials from Carnegie Institution (*68*). The reference materials from Carnegie Institution had been cross-calibrated by multiple independent absolute techniques such as FTIR, elastic recoil detection analysis, and vacuum manometry; see complete list of references in (*68*). Representative calibration curves are presented in fig. S5 and were used to calculate the water and fluorine contents of pyroxenes. Measurements where the internal precision of $^{16}O^1H/^{30}Si$ and/or $^{19}F/^{30}Si$ was greater than 10% were excluded from the dataset. The vast majority of internal 2 SE are much lower than 10%, with an average of 0.4% for OH and 0.8% for F in cpx, and 0.2% for OH and 0.8% for F in opx. These low-precision measurements were typically also associated with elevated C, S, and/or Cl concentrations and are likely the result of analyses conducted on slightly uneven surfaces or nonvisible microfractures. Analytical uncertainties over five counting cycles were combined with calibration slope uncertainties to yield typical total uncertainty (2 SE, 95% confidence intervals) of <5 and <3% for OH and F in cpx, respectively, and <6 and <3% for OH and F in opx, respectively. Continuous measurements of ALV519-4-1 were used throughout the session every couple of hours to monitor instrument drift, which was found to be negligible. The volatile concentrations of Suprasil 102 and Herasil 102 (optical-quality glasses), as well as synthetic forsterite, were measured regularly throughout the session to quantify volatile background abundances. There are no published values for the OH, F, and Cl content of Suprasil 102, Herasil 102, and synthetic forsterite, but those samples are believed to have very low OH, F, and Cl concentrations, respectively (less than a few μg g^{-1}). To quantify our maximum backgrounds, we assume that Suprasil 102 contains no OH, Herasil contains no F, and synthetic forsterite contains no Cl. Background F and Cl values were less than 0.15 and 0.09 μg g^{-1}, respectively, for all sessions. Background OH varied by mount, from ~5 to ~80 μg g^{-1}, in a few samples analyzed at the very beginning of the session (typically 5 to 10 μg g^{-1} when

properly corrected for Si content of glasses; see below). Although most samples were prepared in crystal bound and then mounted in indium specifically for this study, a small subset of samples that we remounted in indium had been previously mounted in epoxy. Not all tiny pieces of epoxy could be removed from all fragile grains, leading to higher backgrounds than when using our usual preparation procedure (*26*, *33*). To ensure proper correction of these few high background measurements, the high background analyses were reanalyzed at a later time when the background was three to four times lower. Several tests have been done to ensure proper correction of the background values, as synthetic glasses and pyroxenes do not have the same composition (e.g., glasses have ~100% SiO_2, while pyroxenes have SiO_2 < 60 wt %). The potential effects of differences in transmission of Si (counts) and composition (Si contents) have been evaluated. Results from the recommended correction method are presented in fig. S6. We recommend that the measured OH contents of Suprasil 102 be conservatively multiplied by 1.85 for opx background and multiplied by 1.95 for cpx background, reflecting the average difference in Si content between the pyroxene and glasses. For example, if the Suprasil 102 background is ~5 μg g^{-1}, it means that the real background is ~9 μg g^{-1} for an opx and ~10 μg g^{-1} for a cpx. By applying this conservative multiplier, we found that volatile values in samples that were initially associated with 60 to 80 μg g^{-1} OH background, and then remeasured with a <20 μg g^{-1} OH background matched the best (closest to a 1:1 line). Without this correction, background values could be slightly underestimated, although it would not change the conclusions of this study. Nevertheless, we recommend that Si-corrected background values should be systematically reported in further volatile studies of minerals by SIMS. Individual mineral analyses were not corrected for background when volatile background values were less than propagated 2 SE uncertainty.

Rare earth elements Sm, Gd, and Yb in selected pyroxenes were analyzed by SIMS with a Cameca IMS 4f ion microprobe at the Istituto di Geoscienze e Georisorse (Pavia) following the method described in a previous study (*22*).

Electron Probe Micro-Analyses

Major element concentrations of pyroxenes were measured with a Cameca SX100 electron probe housed at the American Museum of Natural History (NY) using a 15-kV acceleration voltage, a 20-nA beam, a 10-μm-diameter beam, and 30-s counting times. Sodium and potassium were run under different conditions to attain a higher precision and monitor their mobility, with a 5-nA beam and counting times of 80 s. For details of the method, readers are referred to previous studies (*19*, *22*).

SUPPLEMENTARY MATERIALS

Supplementary material for this article is available at http://advances.sciencemag.org/cgi/content/full/7/24/eabf6071/DC1

REFERENCES AND NOTES

1. S.-I. Karato, M. S. Paterson, J. D. Fitzgerald, Rheology of synthetic olivine aggregates: Influence of grain size and water. *J. Geophys. Res. B Solid Earth* **91**, 8151–8176 (1986).
2. S. J. Mackwell, D. L. Kohlstedt, M. S. Paterson, The role of water in the deformation of olivine single crystals. *J. Geophys. Res. B Solid Earth* **90**, 11319–11333 (1985).
3. S. D. Jacobsen, Effect of water on the equation of state of nominally anhydrous minerals. *Rev. Mineral. Geochem.* **62**, 321–342 (2006).
4. G. Hirth, D. L. Kohlstedt, Water in the oceanic upper mantle: Implications for rheology, melt extraction, and the evolution of the lithosphere. *Earth Planet. Sci. Lett.* **144**, 93–108 (1996).
5. D. G. Pearson, D. Canil, S. B. Shirey, *Treatise on Geochemistry*, D. H. Heinrich, K. T. Karl, Eds. (Pergamon, 2003), pp. 171–275.
6. A. H. Peslier, A review of water contents of nominally anhydrous natural minerals in the mantles of Earth, Mars and the Moon. *J. Volcanol. Geotherm. Res.* **197**, 239–258 (2010).
7. S. Demouchy, N. Bolfan-Casanova, Distribution and transport of hydrogen in the lithospheric mantle: A review. *Lithos* **240-243**, 402–425 (2016).
8. A. H. Peslier, M. Schönbächler, H. Busemann, S.-I. Karato, Water in the Earth's interior: Distribution and origin. *Space Sci. Rev.* **212**, 743–810 (2017).
9. H. Skogby, Water in natural mantle minerals I: Pyroxenes. *Rev. Mineral. Geochem.* **62**, 155–167 (2006).
10. S. Demouchy, S. D. Jacobsen, F. Gaillard, C. R. Stern, Rapid magma ascent recorded by water diffusion profiles in mantle olivine. *Geology* **34**, 429–432 (2006).
11. J. A. O'Leary, G. A. Gaetani, E. H. Hauri, The effect of tetrahedral Al^{3+} on the partitioning of water between clinopyroxene and silicate melt. *Earth Planet. Sci. Lett.* **297**, 111–120 (2010).
12. H. J. B. Dick, R. L. Fisher, W. B. Bryan, Mineralogic variability of the uppermost mantle along mid-ocean ridges. *Earth Planet. Sci. Lett.* **69**, 88–106 (1984).
13. J. M. Warren, E. H. Hauri, Pyroxenes as tracers of mantle water variations. *J. Geophys. Res. Solid Earth* **119**, 1851–1881 (2014).
14. P. Li, Q. K. Xia, L. Dallai, E. Bonatti, D. Brunelli, A. Cipriani, M. Ligi, High H_2O content in pyroxenes of residual mantle peridotites at a Mid Atlantic Ridge segment. *Sci. Rep.* **10**, 579 (2020).
15. E. Schmädicke, J. Gose, R. Stalder, Water in abyssal peridotite: Why are melt-depleted rocks so water-rich? *Geochem. Geophys. Geosyst.* **19**, 1824–1843 (2018).
16. J. Gose, E. Schmädicke, A. Beran, Water in enstatite from Mid-Atlantic Ridge peridotite: Evidence for the water content of suboceanic mantle? *Geology* **37**, 543–546 (2009).
17. K. T. Hesse, J. Gose, R. Stalder, E. Schmädicke, Water in orthopyroxene from abyssal spinel peridotites of the East Pacific Rise (ODP Leg 147: Hess Deep). *Lithos* **232**, 23–34 (2015).
18. E. Bonatti, M. Ligi, D. Brunelli, A. Cipriani, P. Fabretti, V. Ferrante, L. Gasperini, L. Ottolini, Mantle thermal pulses below the Mid-Atlantic Ridge and temporal variations in the formation of oceanic lithosphere. *Nature* **423**, 499–505 (2003).
19. A. Cipriani, E. Bonatti, D. Brunelli, M. Ligi, 26 million years of mantle upwelling below a segment of the Mid Atlantic Ridge: The Vema Lithospheric Section revisited. *Earth Planet. Sci. Lett.* **285**, 87–95 (2009).
20. S. C. Cande, D. V. Kent, Revised calibration of the geomagnetic polarity timescale for the Late Cretaceous and Cenozoic. *J. Geophys. Res. B Solid Earth* **100**, 6093–6095 (1995).
21. C. J. Lissenberg, M. Rioux, N. Shimizu, S. A. Bowring, C. Mével, Zircon dating of oceanic crustal accretion. *Science* **323**, 1048–1050 (2009).
22. D. Brunelli, M. Seyler, A. Cipriani, L. Ottolini, E. Bonatti, Discontinuous melt extraction and weak refertilization of mantle peridotites at the vema lithospheric section (Mid-Atlantic Ridge). *J. Petrol.* **47**, 745–771 (2006).
23. D. Brunelli, A. Cipriani, E. Bonatti, Thermal effects of pyroxenites on mantle melting below mid-ocean ridges. *Nat. Geosci.* **11**, 520–525 (2018).
24. A. Cipriani, E. Bonatti, M. Seyler, H. K. Brueckner, D. Brunelli, L. Dallai, S. R. Hemming, M. Ligi, L. Ottolini, B. D. Turrin, A 19 to 17 Ma amagmatic extension event at the Mid-Atlantic Ridge: Ultramafic mylonites from the Vema Lithospheric Section. *Geochem. Geophys. Geosyst.* **10**, (2009).
25. C. Aubaud, E. H. Hauri, M. M. Hirschmann, Hydrogen partition coefficients between nominally anhydrous minerals and basaltic melts. *Geophys. Res. Lett.* **31**, L20611 (2004).
26. B. M. Urann, V. Le Roux, K. Hammond, H. R. Marschall, C.-T. A. Lee, B. D. Monteleone, Fluorine and chlorine in mantle minerals and the halogen budget of the Earth's mantle. *Contrib. Mineral. Petrol.* **172**, 51 (2017).
27. J. M. Warren, Global variations in abyssal peridotite compositions. *Lithos* **248–251**, 193–219 (2016).
28. A. W. Ashley, M. Bizimis, A. H. Peslier, M. Jackson, J. Konter, Metasomatism and hydration of the oceanic lithosphere: A case study of peridotite xenoliths from Samoa. *J. Petrol.* **61**, egaa028 (2020).
29. P. J. Michael, The concentration, behavior, and storage of H_2O in the suboceanic upper mantle: Implications for mantle metasomatism. *Geochim. Cosmochim. Acta* **52**, 555–566 (1988).
30. E. Anders, N. Grevesse, Abundances of the elements—Meteoritic and solar. *Geochim. Cosmochim. Acta* **53**, 197–214 (1989).
31. R. K. Workman, S. R. Hart, Major and trace element composition of the depleted MORB mantle (DMM). *Earth Planet. Sci. Lett.* **231**, 53–72 (2005).
32. A. E. Saal, E. H. Hauri, C. H. Langmuir, M. R. Perfit, Vapour undersaturation in primitive mid-ocean-ridge basalt and the volatile content of Earth's upper mantle. *Nature* **419**, 451–455 (2002).
33. B. M. Urann, V. Le Roux, T. John, B. G. M, J. D. Barnes, The distribution and abundance of halogens in eclogites: An in situ SIMS perspective of the Raspas Complex (Ecuador). *Am. Mineral.* **105**, 307–318 (2020).
34. E. H. Hauri, G. A. Gaetani, T. H. Green, Partitioning of water during melting of the Earth's upper mantle at H_2O-undersaturated conditions. *Earth Planet. Sci. Lett.* **248**, 715–734 (2006).

35. E. Hellebrand, J. E. Snow, P. Hoppe, A. W. Hofmann, Garnet-field melting and late-stage refertilization in 'residual' abyssal peridotites from the Central Indian Ridge. *J. Petrol.* **43**, 2305–2338 (2002).
36. C. Crépisson, M. Blanchard, H. Bureau, C. Sanloup, A. C. Withers, H. Khodja, S. Surblé, C. Raepsaet, K. Béneut, C. Leroy, P. Giura, E. Balan, Clumped fluoride-hydroxyl defects in forsterite: Implications for the upper mantle. *Earth Planet. Sci. Lett.* **390**, 287–295 (2014).
37. K. J. Lynn, J. M. Warren, The potential for aqueous fluid-rock and silicate melt-rock interactions to re-equilibrate hydrogen in peridotite nominally anhydrous minerals. *Am. Mineral.* **106**, 701–714 (2020).
38. L. A. Schaffer, A. H. Peslier, A. D. Brandon, M. Bizimis, R. Gibler, M. Norman, J. Harvey, Effects of melting, subduction-related metasomatism, and sub-solidus equilibration on the distribution of water contents in the mantle beneath the Rio Grande Rift. *Geochim. Cosmochim. Acta* **266**, 351–381 (2019).
39. C. Aubaud, M. M. Hirschmann, A. C. Withers, R. L. Hervig, Hydrogen partitioning between melt, clinopyroxene, and garnet at 3 GPa in a hydrous MORB with 6 wt.% H_2O. *Contrib. Mineral. Petrol.* **156**, 607–625 (2008).
40. C. G. Sun, Y. Liang, Distribution of REE between clinopyroxene and basaltic melt along a mantle adiabat: Effects of major element composition, water, and temperature. *Contrib. Mineral. Petrol.* **163**, 807–823 (2012).
41. G. P. Brey, T. Köhler, Geothermobarometry in four-phase lherzolites II. New thermobarometers, and practical assessment of existing thermobarometers. *J. Petrol.* **31**, 1353–1378 (1990).
42. V. Le Roux, J.-L. Bodinier, A. Tommasi, O. Alard, J.-M. Dautria, A. Vauchez, A. J. V. Riches, The Lherz spinel lherzolite: Refertilized rather than pristine mantle. *Earth Planet. Sci. Lett.* **259**, 599–612 (2007).
43. E. Ferriss, T. Plank, D. Walker, Site-specific hydrogen diffusion rates during clinopyroxene dehydration. *Contrib. Mineral. Petrol.* **171**, 55 (2016).
44. R. Sundvall, H. Skogby, Hydrogen defect saturation in natural pyroxene. *Phys. Chem. Miner.* **38**, 335–344 (2011).
45. Y. Xu, W. Tang, H. Hui, R. L. Rudnick, S. Shang, Z. Zhang, Reconciling the discrepancy between the dehydration rates in mantle olivine and pyroxene during xenolith emplacement. *Geochim. Cosmochim. Acta* **267**, 179–195 (2019).
46. J. A. Van Orman, T. L. Grove, N. Shimizu, Rare earth element diffusion in diopside: Influence of temperature, pressure, and ionic radius, and an elastic model for diffusion in silicates. *Contrib. Mineral. Petrol.* **141**, 687–703 (2001).
47. R. Stalder, H. Skogby, Hydrogen diffusion in natural and synthetic orthopyroxene. *Phys. Chem. Miner.* **30**, 12–19 (2003).
48. A. J. Berry, H. S. C. O'Neill, J. Hermann, D. R. Scott, The infrared signature of water associated with trivalent cations in olivine. *Earth Planet. Sci. Lett.* **261**, 134–142 (2007).
49. Q. Bai, D. L. Kohlstedt, Effects of chemical environment on the solubility and incorporation mechanism for hydrogen in olivine. *Phys. Chem. Miner.* **19**, 460–471 (1993).
50. A. Nakamura, H. Schmalzried, On the nonstoichiometry and point defects of olivine. *Phys. Chem. Miner.* **10**, 27–37 (1983).
51. D. R. Bell, G. R. Rossman, R. O. Moore, Abundance and partitioning of OH in a high-pressure magmatic system: Megacrysts from the Monastery Kimberlite, South Africa. *J. Petrol.* **45**, 1539–1564 (2004).
52. J. R. Holloway, B. J. Wood, *Simulating the Earth: Experimental Geochemistry*, J. R. Holloway, B. J. Wood, Eds. (Springer Netherlands, 1988), pp. 143–168.
53. H. Skogby, OH incorporation in synthetic clinopyroxene. *Am. Mineral.* **79**, 240–249 (1994).
54. A. H. Peslier, J. F. Luhr, J. Post, Low water contents in pyroxenes from spinel-peridotites of the oxidized, sub-arc mantle wedge. *Earth Planet. Sci. Lett.* **201**, 69–86 (2002).
55. S. J. Mackwell, Q. Bai, D. L. Kohlstedt, Rheology of olivine and the strength of the lithosphere. *Geophys. Res. Lett.* **17**, 9–12 (1990).
56. P. Tollan, J. Hermann, Arc magmas oxidized by water dissociation and hydrogen incorporation in orthopyroxene. *Nat. Geosci.* **12**, 667–671 (2019).
57. D. J. Frost, C. A. McCammon, The redox state of Earth's mantle. *Annu. Rev. Earth Planet. Sci.* **36**, 389–420 (2008).
58. F. A. Davis, E. Cottrell, S. K. Birner, J. M. Warren, O. G. Lopez, Revisiting the electron microprobe method of spinel-olivine-orthopyroxene oxybarometry applied to spinel peridotites. *Am. Mineral.* **102**, 421–435 (2017).
59. J. R. Smyth, D. R. Bell, G. R. Rossman, Incorporation of hydroxyl in upper-mantle clinopyroxenes. *Nature* **351**, 732–735 (1991).
60. P. M. E. Tollan, H. S. C. O'Neill, J. Hermann, The role of trace elements in controlling H incorporation in San Carlos olivine. *Contrib. Mineral. Petrol.* **173**, 89 (2018).
61. A. H. Peslier, M. Bizimis, Water in Hawaiian peridotite minerals: A case for a dry metasomatized oceanic mantle lithosphere. *Geochem. Geophys. Geosyst.* **16**, 1211–1232 (2015).
62. M. Le Voyer, E. H. Hauri, E. Cottrell, K. A. Kelley, V. J. M. Salters, C. H. Langmiur, D. R. Hilton, P. H. Barry, E. Furi, Carbon fluxes and primary magma CO_2 contents along the global mid-ocean ridge system. *Geochem. Geophys. Geosyst.* **20**, 1387–1424 (2019).
63. M. Ligi, E. Bonatti, A. Cipriani, L. Ottolini, Water-rich basalts at mid-ocean-ridge cold spots. *Nature* **434**, 66–69 (2005).
64. T. Keller, R. F. Katz, M. M. Hirschmann, Volatiles beneath mid-ocean ridges: Deep melting, channelised transport, focusing, and metasomatism. *Earth Planet. Sci. Lett.* **464**, 55–68 (2017).
65. M. Seyler, M. Toplis, J. P. Lorand, A. Luguet, M. Cannat, Clinopyroxene microtextures reveal incompletely extracted melts in abyssal peridotites. *Geology* **29**, 155–158 (2001).
66. T. Hiraga, I. M. Anderson, D. L. Kohlstedt, Grain boundaries as reservoirs of incompatible elements in the Earth's mantle. *Nature* **427**, 699–703 (2004).
67. Y. L. Niu, Bulk-rock major and trace element compositions of abyssal peridotites: Implications for mantle melting, melt extraction and post-melting processes beneath mid-ocean ridges. *J. Petrol.* **45**, 2423–2458 (2004).
68. K. M. Kumamoto, J. M. Warren, E. H. Hauri, New SIMS reference materials for measuring water in upper mantle minerals. *Am. Mineral.* **102**, 537–547 (2017).
69. C. Beyer, S. Klemme, M. Wiedenbeck, A. Stracke, C. Vollmer, Fluorine in nominally fluorine-free mantle minerals: Experimental partitioning of F between olivine, orthopyroxene and silicate melts with implications for magmatic processes. *Earth Planet. Sci. Lett.* **337–338**, 1–9 (2012).

Acknowledgments: We thank an anonymous reviewer, L. Doucet, C. Langmuir, and P. Tollan for thoughtful reviews that improved this manuscript. We thank B. Schoene for editorial handling of the manuscript. **Funding:** Funding for this study was supported by NSF EAR-P&G 1524311 and 1839128 to V.L.R. and the Andrew W. Mellon Foundation Award for Innovative Research to V.L.R. A.C. and D.B. were funded by the Italian Programma di Rilevante Interesse Nazionale PRIN 20178LPCPW and PRIN2017KY5ZX8, respectively. Revisions were performed within the duration of a "Visiting Scholar at SCIENCE 2020" award to V.L.R. (University of Copenhagen, Denmark), with support from the Department of Geosciences and Natural Resource Management, Section for Geology. **Author contributions:** V.L.R. designed the study and wrote the manuscript. V.L.R. and B.M.U. performed the volatile analyses by SIMS at WHOI. E.B., D.B., and A.C. provided the samples and performed major and trace element analyses. S.D. contributed to the discussion on diffusional processes. B.D.M. assisted with technical developments of SIMS analyses at WHOI. All coauthors commented on the manuscript. **Competing interests:** The authors declare that they have no competing interests. **Data and materials availability:** All data needed to evaluate the conclusions in the paper are present in the paper and/or the Supplementary Materials. Additional data related to this paper may be requested from the authors.

Submitted 6 November 2020
Accepted 21 April 2021
Published 9 June 2021
10.1126/sciadv.abf6071

Citation: V. Le Roux, B. M. Urann, D. Brunelli, E. Bonatti, A. Cipriani, S. Demouchy, B. D. Monteleone, Postmelting hydrogen enrichment in the oceanic lithosphere. *Sci. Adv.* **7**, eabf6071 (2021).

ScienceAdvances

Postmelting hydrogen enrichment in the oceanic lithosphere

Veronique Le RouxBenjamin M. UrannDaniele BrunelliEnrico BonattiAnna CiprianiSylvie DemouchyBrian D. Monteleone

Sci. Adv., 7 (24), eabf6071. • DOI: 10.1126/sciadv.abf6071

Science Advances (ISSN 2375-2548) is published by the American Association for the Advancement of Science. 1200 New York Avenue NW, Washington, DC 20005. The title *Science Advances* is a registered trademark of AAAS.